

# Heat Transfer across the Interface between Nanoscale Solids and Gas

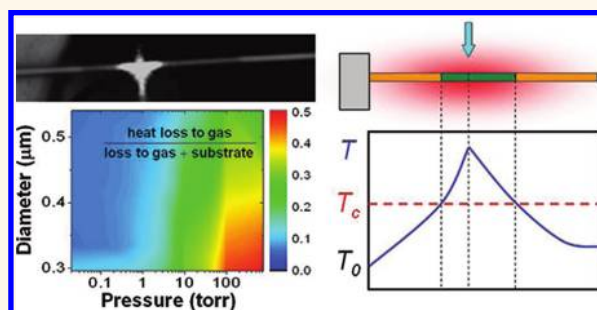
Chun Cheng,<sup>†,‡</sup> Wen Fan,<sup>†,\*,‡</sup> Jinbo Cao,<sup>§</sup> Sang-Gil Ryu,<sup>⊥</sup> Jie Ji,<sup>‡</sup> Costas P. Grigoropoulos,<sup>⊥</sup> and Junqiao Wu<sup>†,§,\*</sup>

<sup>†</sup>Department of Materials Science and Engineering, University of California, Berkeley, California 94720, United States, <sup>‡</sup>Department of Thermal Science and Energy Engineering, University of Science and Technology of China, Hefei, China, <sup>§</sup>Materials Sciences Division, Lawrence Berkeley National Laboratory, Berkeley, California 94720, United States, and <sup>⊥</sup>Department of Mechanical Engineering, University of California, Berkeley, California 94720, United States. \*These authors contributed equally to the work.

As electronic devices continue to scale down in dimension and scale up in power density, thermal management becomes a critical issue to ensure high device performance. New thermal physics also emerges when the size of the active region becomes comparable to certain characteristic lengths. For example, in the near field, heat loss through radiation can be several orders of magnitude higher than far-field radiation;<sup>1–3</sup> in nanostructures with size or surface roughness comparable to the phonon mean free path, their lattice thermal conductivity may be much reduced from their bulk counterparts.<sup>4–7</sup> Relative to heat transferred *via* solid–solid interfaces, heat dissipation from the active device region to the gas environment is usually negligible. However, in nanoscale materials and devices of high surface-to-volume ratios, the latter becomes increasingly important because it occurs at all exposed surfaces, while the heat transfer to solid substrate is limited by the area and thermal quality of the solid interface. Moreover, in many device applications where the active device component needs to be suspended, the heat loss *via* surface becomes even more important, such as nanowire (NW)-based lasers,<sup>8,9</sup> field emitters,<sup>10</sup> gas sensors,<sup>11</sup> antennas,<sup>12</sup> oscillators,<sup>13</sup> and microelectromechanical systems.<sup>14</sup> In these applications, heat loss through exchanging energy with gaseous environment can be also exploited as an effective device cooling mechanism.<sup>15</sup>

Heat transfer across a hot solid surface and the gas environment at the macroscopic scale is a well understood phenomenon, on which numerous experiments have been done and empirical and analytical equations were proposed based on the kinetic theory of gas.<sup>16</sup> However, there has been little exploration to quantitatively determine the heat transfer across the interface of submicrometer solids and gas. This is

## ABSTRACT



When solid materials and devices scale down in size, heat transfer from the active region to the gas environment becomes increasingly significant. We show that the heat transfer coefficient across the solid–gas interface behaves very differently when the size of the solid is reduced to the nanoscale, such as that of a single nanowire. Unlike for macroscopic solids, the coefficient is strongly pressure dependent above  $\sim 10$  Torr, and at lower pressures it is much higher than predictions of the kinetic gas theory. The heat transfer coefficient was measured between a single, free-standing  $\text{VO}_2$  nanowire and surrounding air using laser thermography, where the temperature distribution along the  $\text{VO}_2$  nanowire was determined by imaging its domain structure of metal–insulator phase transition. The one-dimensional domain structure along the nanowire results from the balance between heat generation by the focused laser and heat dissipation to the substrate as well as to the surrounding gas, and thus serves as a nanoscale power-meter and thermometer. We quantified the heat loss rate across the nanowire–air interface, and found that it dominates over all other heat dissipation channels for small-diameter nanowires near ambient pressure. As the heat transfer across the solid–gas interface is nearly independent of the chemical identity of the solid, the results reveal a general scaling relationship for gaseous heat dissipation from nanostructures of all solid materials, which is applicable to nanoscale electronic and thermal devices exposed to gaseous environments.

**KEYWORDS:** heat transfer · solid – gas (vapor) interface · nanowire · vanadium dioxide · phase transition · conduction and convection

largely due to difficulties in accurate determination of power consumption and temperature distribution at this scale without interfering with the thermal flow. Decoupling the heat loss to the gas from that to the supporting substrate is also a practical challenge. Measuring and fundamental understanding of the heat exchange across the solid–gas interface at the submicrometer

\* Address correspondence to wuj@berkeley.edu.

Received for review October 22, 2011 and accepted November 9, 2011.

Published online November 09, 2011  
10.1021/nn204072n

© 2011 American Chemical Society

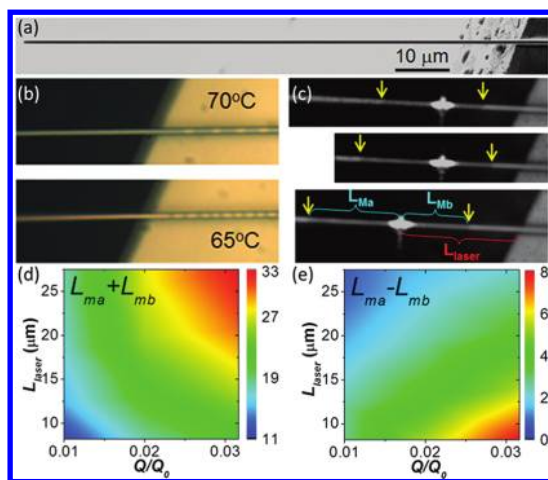


**Figure 1.** (a) SEM image of a VO<sub>2</sub> NW cantilever grown out the edge of a Si substrate. (b) Optical images of the NW at substrate temperatures below or above the phase transition temperature. (c) Optical images of the NW when a laser is focused at the NW at a distance  $L_{\text{laser}}$  from the root of the NW. The M-phase domain (dark) is clearly resolved from the I-phase (bright). Arrows show location of the M–I domain walls. The laser power  $Q$  and laser focus position  $L_{\text{laser}}$  are, from top to bottom panel, ( $10^{-2}Q_0$ ,  $7.16 \mu\text{m}$ ), ( $10^{-1.8}Q_0$ ,  $7.16 \mu\text{m}$ ), ( $10^{-1.8}Q_0$ ,  $12.48 \mu\text{m}$ ), where  $Q_0$  is determined to be 3.3 mW by fitting theory to the full set of experimental data. (d) Measured total length of M domain ( $L_{\text{Ma}} + L_{\text{Mb}}$ ) as a function of laser position  $L_{\text{laser}}$  and relative laser power  $Q/Q_0$ . (e) The asymmetry of M domain ( $L_{\text{Ma}} - L_{\text{Mb}}$ ) as a function of  $L_{\text{laser}}$  and  $Q/Q_0$ . In panels d and e, the measured discrete data are interpolated to render a continuous color plot.

scale becomes an urgent yet challenging research topic.

Here we demonstrate an effective way to measure the heat transfer coefficient ( $h$ ) between a single NW and gas environment using laser thermography. Long VO<sub>2</sub> NWs were cantilevered from a substrate and were locally heated using a focused laser, allowing the laser-heating induced phase transition and the resultant domain structures along the NW to be optically imaged. By comparing to heat transport theory, we determined  $h$  as a function of gas pressure and the NW diameter. We found that  $h$  behaves very differently from that between macroscopic solids and gas, and at low pressures is much higher than what is predicted by the kinetic gas theory. We also quantified the contribution of heat transfer across the NW–air interface compared to other heat dissipation channels, and found that it becomes dominant for small-diameter NWs near ambient pressure.

## RESULTS AND DISCUSSION

At the strain-free state, VO<sub>2</sub> undergoes a first-order metal (M) to insulator (I) transition (MIT) at  $T_C = 68 \text{ }^\circ\text{C}$  with a drastic change in electric conductivity and optical reflectivity.<sup>17</sup> The electronic transition is accompanied with a structural transition from the high-temperature, tetragonal phase to the low-temperature, monoclinic phase.<sup>18</sup> Under white light illumination, the M phase shows dark reflection while the I phase appears bright.<sup>19</sup> As strain has complicated effects on

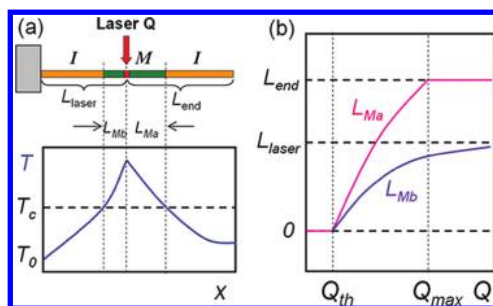


**Figure 2.** (a) Schematic view of the steady state of a VO<sub>2</sub> cantilever under focused laser heating. The lower panel shows schematically the temperature distribution according to the solution of eq 2. (b) The solution schematics of  $L_{\text{Ma}}$  and  $L_{\text{Mb}}$  as predicted by eq 4.

the MIT of VO<sub>2</sub>,<sup>20</sup> strain-free crystals can serve as a clean system to probe and exploit the MIT of VO<sub>2</sub>. We synthesized single-crystal VO<sub>2</sub> NWs on a Si surface using the vapor transport method reported previously.<sup>21</sup> The Si surface is coated with 100 nm thick thermal SiO<sub>2</sub>. These NWs grow along the  $c_R$ -axis with  $\{110\}_R$  planes as bounding facets (therefore rectangular cross section), and have widths below a micrometer and lengths over 100  $\mu\text{m}$ .<sup>21</sup> Some of them grow out of the edge of the substrate forming strain-free NW cantilevers. The roots of these NWs are long and half-embedded into the substrate, forming good thermal contact. Figure 1a,b show images of such a VO<sub>2</sub> NW cantilever, which is in the I phase at low temperatures and abruptly switches to the M phase above  $T_C$ .

A continuous-wave laser is focused to a spot with diameter of  $\sim 2 \mu\text{m}$  and locally heats the NW cantilever, as shown in Figure 1c. The portion near the laser spot switches to the M phase (dark reflection), while the rest remains in the I phase because of heat dissipation to the substrate and to the surrounding air. The M domains at the two sides of the laser spot have different lengths (defined as  $L_{\text{Ma}}$  and  $L_{\text{Mb}}$ , respectively) due to heat transfer to the substrate. Figure 1d, e show  $L_{\text{Ma}}$  and  $L_{\text{Mb}}$  as a function of the power ( $Q$ ) and position ( $L_{\text{laser}}$ ) of the focused laser beam. To highlight the asymmetry in  $L_{\text{Ma}}$  and  $L_{\text{Mb}}$ , the total M domain length ( $L_{\text{Ma}} + L_{\text{Mb}}$ ) and the asymmetry ( $L_{\text{Ma}} - L_{\text{Mb}}$ ) are plotted separately. It can be seen that both  $L_{\text{Ma}} + L_{\text{Mb}}$  and  $L_{\text{Ma}} - L_{\text{Mb}}$  are sensitive to  $Q$  and  $L_{\text{laser}}$ , but with distinctly different dependences. Here  $Q$  is shown as a dimensionless quantity of  $Q/Q_0$ , where  $Q_0$  is a common factor of laser power in the experiments. This is because when  $Q$  is varied, the absolute value of  $Q$  is unknown; instead, we only know the ratio between different  $Q$  values from the optical attenuators used. As discussed below, however,  $Q_0$  can be determined by fitting theoretical predications of  $L_{\text{Ma}}$  and  $L_{\text{Mb}}$  to experimental data.

According to the heat transport theory, the temperature profile outside the laser spot in such a quasi-one-dimensional thermal system with NW width  $a$ , height  $b$ ,

and total length  $L$  is given by (Figure 2a,b)

$$\rho c \frac{\partial T(x,t)}{\partial t} = \kappa \frac{\partial^2 T(x,t)}{\partial x^2} - 2h \frac{a+b}{ab} [T(x,t) - T_0] - R_{\text{radiation}} \quad (1)$$

where  $\rho$ ,  $c$ , and  $\kappa$  are the density, specific heat, and thermal conductivity of the NW, respectively.  $R_{\text{radiation}}$  is heat dissipation through radiation;  $T_0$  is the environment temperature (27 °C);  $h$  is the total heat transfer coefficient to air *via* conduction and convection. At low temperatures like ours (less than  $\sim 100$  °C), the radiation term is several orders of magnitude smaller than the other terms. In steady state the equation can be simplified as

$$\kappa \frac{d^2 T(x)}{dx^2} - 2h \frac{a+b}{ab} [T(x) - T_0] = 0 \quad (2)$$

The boundary conditions are

$$\begin{aligned} T(x) |_{x=0} &= T_0, \\ dT(x)/dx |_{x=L} &= 0, \quad ab\kappa [-dT(x)/dx |_{x=L_{\text{laser}}} + \\ &+ dT(x)/dx |_{x=L_{\text{laser}}}] = Q \end{aligned} \quad (3)$$

We ignore the finite size of laser spot because it is much smaller than  $L_{\text{laser}}$  and the M domain lengths. Equation 2 is solved analytically and the solution  $T(x)$  is compared to  $T_C$ , which defines the M domain in the portion with  $T(x) > T_C$ . The lengths of M domain to the left and right side of the laser spot are (Figure 2b),

$$\begin{aligned} L_{\text{Mb}} &= -\frac{1}{m} \ln \left[ \frac{abmn_a \kappa (T_C - T_0)}{Q} \right. \\ &\left. + \sqrt{\left( \frac{abmn_a \kappa (T_C - T_0)}{Q} \right)^2 + e^{-2mL_{\text{laser}}}} \right] \end{aligned}$$

and

$$\begin{aligned} L_{\text{Ma}} &= \frac{1}{m} \ln \left[ \frac{abmn_b \kappa (T_C - T_0)}{Q} \right. \\ &\left. - \sqrt{\left( \frac{abmn_b \kappa (T_C - T_0)}{Q} \right)^2 - e^{2mL_{\text{end}}}} \right] \end{aligned} \quad (4)$$

where  $m = (2h(a+b)/ab\kappa)^{1/2}$ ,  $L_{\text{end}} = L - L_{\text{laser}}$ ,  $n_a = (e^{2mL_{\text{end}}} + e^{-2mL_{\text{laser}}})/(1 + e^{2mL_{\text{end}}})$ , and  $n_b = (e^{2mL_{\text{end}}} + e^{-2mL_{\text{laser}}})/(1 - e^{-2mL_{\text{laser}}})$ . From these solutions it can be seen that the laser power  $Q$  needs to be higher than  $Q_{\text{th}} \equiv 2abmn\kappa(T_C - T_0)$  in order to have a nonzero M domain length, where  $n = (e^{2mL_{\text{end}}} + e^{-2mL_{\text{laser}}})/[(1 - e^{-2mL_{\text{laser}}})(1 + e^{2mL_{\text{end}}})]$ . As  $Q$  increases from  $Q_{\text{th}}$ , both  $L_{\text{Ma}}$  and  $L_{\text{Mb}}$  grow from zero.  $L_{\text{Ma}}$  reaches  $L_{\text{end}}$  at  $Q = Q_{\text{max}} \equiv abmn_b \kappa e^{-mL_{\text{end}}}(T_C - T_0)$ , while  $L_{\text{Mb}}$  continues to increase and theoretically reaches the value of  $L_{\text{laser}}$  at  $Q \rightarrow \infty$ . We observed that even at the strongest safe  $Q$  and small  $L_{\text{laser}}$ , the M domain never reaches the root of the NW, which confirms the good thermal contact with the substrate and justifies the boundary condition of  $T(x)|_{x=0} = T_0$ .

The calculated  $L_{\text{Ma}}$  and  $L_{\text{Mb}}$  as a function of a wide range of  $Q$  and  $L_{\text{laser}}$  are fitted to the measured data using  $h$  and  $Q_0$  as the only fitting parameters. The thermal conductivity of  $\text{VO}_2$  is assumed to be a constant for both the M and I phases, 6.5W/mK, taken from the literature.<sup>17</sup> The best, simultaneous fit to both  $L_{\text{Ma}}$  and  $L_{\text{Mb}}$  at various  $L_{\text{laser}}$  and  $Q/Q_0$  values yields the value of  $h$  for a range of  $P$  and  $D$ , as shown in Figure 3a, b. Here  $D$  is the characteristic width of the NW defined as  $D = 2ab/(a+b)$ , which is proportional to the volume-to-surface ratio of the NW. As  $P$  increases from 0.02 to 760 Torr,  $h$  first increases rapidly and then slows down after 100 Torr. According to the kinetic theory of gas,<sup>16</sup> the heat transfer between a solid surface and gas can be divided into two regimes, the fluidic (continuous) flow regime where the Knudsen number  $K_n \ll 1$ , and the molecular (ballistic) flow regime where  $K_n \gg 1$ . Here the Knudsen number is defined as  $K_n = L_{\text{MFP}}/D$ , where  $L_{\text{MFP}}$  is the mean free path of the gas molecules and equal to  $k_B T/2^{1/2} \pi d_g^2 P \equiv c/P$  for an ideal gas ( $d_g$  is the average diameter of gas molecules).  $K_n \approx 1$  defines a situation in which the collision among gas molecules occurs equally frequently compared to the collision between the gas molecules and the exposed solid surface. It can be estimated that for the NWs with submicrometer widths, the transition between the fluidic and the molecular regimes ( $K_n \approx 1$ ) occurs at  $P \approx 100$  Torr, which agrees with the pressure at which  $h$  changes behavior in Figure 3a.

The heat transfer coefficient between a hot surface and gas has been usually measured in the Dickins geometry,<sup>22</sup> in which a hot, long wire with diameter  $D$  is suspended along the axis of a cold cylinder that has radius  $R$  and is filled with gas at pressure  $P$ . In this configuration it is shown that the heat transfer coefficient from the hot wire is given by<sup>16</sup>

$$h(P, D) = \frac{\alpha \cdot \kappa_{\text{gas}}}{D \ln(R/D) + (c/P)(D/R + 1)} \quad (5)$$

where  $c$  is the coefficient linking the molecular mean free path  $L_{\text{MFP}}$  and  $1/P$ , and  $\kappa_{\text{gas}}$  is the gas heat conduction coefficient, which is equal to  $(5k_B(k_B T)^{1/2})/(2\pi d_g^2(\pi M)^{1/2})$  for an ideal gas, where  $M$  is the molecular mass of the gas.<sup>23</sup> If the experimental configuration is different from the Dickins geometry,  $R$  should be the average distance between the hot surface and the cold wall where the gas molecules reject the heat (assuming  $R \gg D$ ); in this situation a numerical coefficient  $\alpha$  is introduced to account for the difference in geometry.

From eq 5 it can be seen that at low pressures (molecule flow regime,  $K_n \gg 1$ ,  $L_{\text{MFP}} \gg D$ ),  $h$  is proportional to  $P$ , and insensitive to  $D$ . This is because the gas density is so low that all molecules directly carry heat away from the hot surface *via* single collisions to the surface; therefore  $h$  is proportional to the frequency of molecular collision at the hot surface ( $\propto P$ ) and the molar heat capacity of molecules (independent of  $P$ ). In

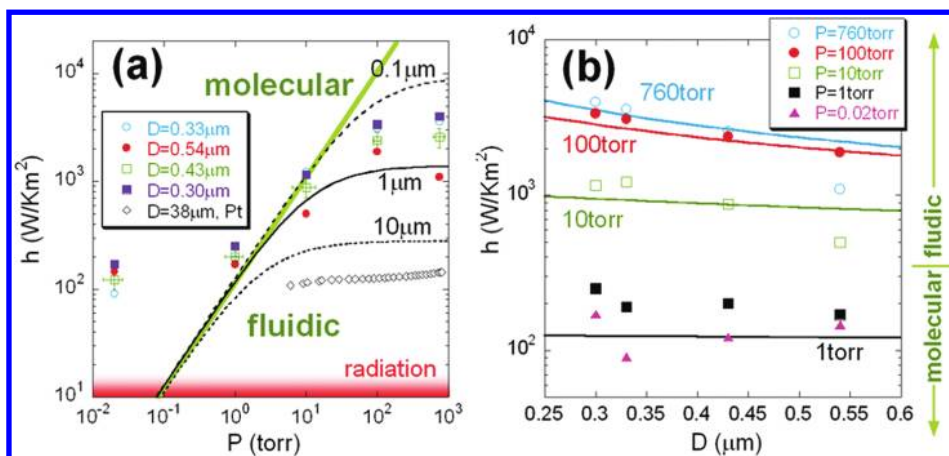


Figure 3. The measured heat transfer coefficient  $h$  as a function of (a) gas pressure  $P$  and (b) characteristic size  $D$  of the NW. In panels a and b, the lines are calculated dependence from eq 5. The estimated contribution of radiative heat loss is shown in panel a. For comparison, data of a thick Pt wire with  $D = 38 \mu\text{m}$  (from ref 16) is also shown in panel a. The error bars in panel a show the approximate range of error for all the data points, and primarily originate from uncertainties in measuring the M domain lengths, the NW width,  $Q/Q_0$ , and the  $T_c$  hysteresis ( $\sim 2^\circ\text{C}$ ).

contrast, at high pressures (fluidic flow regime,  $K_n \ll 1$ ,  $L_{\text{MFP}} \ll D$ ),  $h$  is independent of  $P$ , and sensitive to  $D$ . This is the regime where the incident gas molecules reach quasi-thermal equilibrium with themselves and with the hot surface *via* multiple collisions. The heat transfer rate is then proportional to the total number of incident molecules within the distance of  $L_{\text{MFP}}$  away from the surface, which is the product of the molecular density ( $\propto P$ ) and the mean free path ( $L_{\text{MFP}} \propto 1/P$ ).<sup>23</sup> This results in the independence of  $h$  from  $P$ . Equation 5 takes into account the conductive heat loss only, while the radiative and convective heat losses are not included. From the Stefan–Boltzmann law of blackbody radiation, the radiative energy loss can be estimated to be extremely low for our system as the maximum temperature involved is below  $\sim 100^\circ\text{C}$ . The resultant contribution of radiation to the measured  $h$  is estimated to be  $\sim 10 \text{ W/Km}^2$ , as shown in Figure 3a. For heat transport due to free air convection, it has been shown experimentally by Langmuir<sup>24</sup> and Brody and Korosy<sup>25</sup> that the contribution of convection to  $h$  at ambient condition is 10 times lower than that of the air conduction. We therefore use eq 5 as the basis to analyze our experimental data.

Figure 3 shows the calculated  $h$  as a function of  $P$  and  $D$  using eq 5. In the calculation, the average distance between the hot surface and the heat sink ( $R$ ) is taken to be on the order of the length of the  $\text{VO}_2$  NW ( $\sim 100 \mu\text{m}$ ), because the Si substrate is the closest surface where the gas molecules reject the heat. Air conductivity of  $\kappa_{\text{gas}} = 0.026 \text{ W/mK}$  was used,<sup>26</sup> and  $\alpha$  was adjusted to obtain the simultaneous fitting to all the data of various  $D$ . It can be seen that eq 5 well describes the data at midhigh pressures ( $P > 1 \text{ Torr}$ ). For comparison, Figure 3a also show data from a macroscopically thick Pt wire (radius =  $38 \mu\text{m}$ ) measured in Dickins' original study.<sup>16</sup> It can be seen that both the data of

macroscopic wire and NWs form a consistent trend agreeing with eq 5. The distinct difference of NWs from macroscopic objects is that the  $h$  of NWs exhibit a much stronger  $P$  dependence at subambient pressures (10–760 Torr). This is understood considering that these pressures are completely in the fluidic regime for macroscopic objects, but not for NWs.

Second, for pressures below 1 Torr,  $h$  is significantly higher than the prediction of eq 5. At  $P = 0.02 \text{ Torr}$ ,  $h$  is near  $100 \text{ W/Km}^2$  while eq 5 predicts a 2 orders of magnitude lower value of  $\sim 1 \text{ W/Km}^2$ . This discrepancy puts in question the validity of eq 5 at the nanoscale at low pressures. In this pressure regime, the mean free path  $L_{\text{MFP}}$  is large and becomes comparable to the macroscopic average distance between the hot surface and the heat sink ( $R \sim 100 \mu\text{m}$ ). It is likely that in this situation the free air convection around the solid surface, which is ignored in eq 5, starts to dominate the heat exchange and results in  $h$  much higher than the prediction of eq 5. Note that in concluding that heat loss carried by free air convection is negligible at ambient condition, Langmuir<sup>24</sup> assumes the existence of a stationary air film around the solid surface which transports heat away conductively. When the mean free path of the gas molecules  $L_{\text{MFP}}$  is comparable to the macroscopic length  $R$ , this assumption is questionable and possibly causes relatively strong convective heat loss. In fact, for external free air convection around a macroscopic, horizontal cylinder, the heat transfer coefficient is given by a Nusselt number,  $Nu$ , as<sup>27</sup>

$$h = Nu\kappa_{\text{gas}}/D \quad (6)$$

where  $Nu$  is on the order of 20. Attempt to apply this equation to the NWs in this study results in an  $h$  on the order of  $10^6 \text{ W/Km}^2$ , much higher than all the measured values in Figure 3. The discrepancies between measured  $h$  and the predicted by both pure

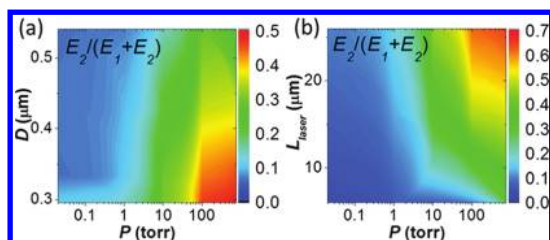


**Figure 4.** (a) Experimentally determined fraction of heat loss to air compared to total heat loss of the NW, as a function of pressure  $P$  and characteristic size  $D$  of NW. Here  $L_{\text{laser}}$  is fixed at  $15 \mu\text{m}$ . (b) The fraction at different laser focus position and pressure  $P$ . Here  $D$  is  $0.33 \mu\text{m}$ .

conduction (eq 5) and pure convection (eq 6) highlight the complication of heat transfer across the surface of submicrometer solids. It is therefore clear that kinetic theories of heat exchange between gas and macroscopic surface, such as eqs 5 and 6, need to be revisited when applied to nanoscale solids. An intriguing point is to examine the behavior of gas viscosity when it interfaces nanoscale solid surfaces, because it is the gas viscosity that determines the degree of gas convection. For an ideal gas, the classical kinetic gas theory predicts a viscosity given by  $NM\bar{v}L_{\text{MFP}}/4 \propto (MT)^{1/2}/d_{\text{gr}}^2$ , independent of pressure and the solid size, where  $N$  is the number density of gas molecules. When the solid size is comparable or smaller than  $L_{\text{MFP}}$ , the viscosity behavior of the surrounding gas needs to be re-examined.

It is practically interesting to compare the rate of heat loss to air ( $E_2$ ) with that to the substrate ( $E_1$ ). Figure 4 shows the experimentally determined fraction of  $E_2$  in the total heat loss,  $f = E_2/(E_1 + E_2)$ , as a function of  $P$ ,  $D$ , and  $L_{\text{laser}}$ . It can be seen that  $f$  can become a dominant heat loss mechanism in certain conditions, specifically, at high pressures, with small-diameter NWs, and when the heat source is far from the substrate. Especially, at ambient pressure,  $f$  exceeds 50% for  $L_{\text{laser}} > 15 \mu\text{m}$  and  $D < 0.3 \mu\text{m}$ . The increase in  $f$  with decreasing  $D$  is clearly due to the fact that  $E_2$  is a surface effect scaling with  $D$ , while  $E_1$  is a volumetric effect scaling with the wire cross section  $D^2$ . As the heat transfer across the solid–gas interface depends primarily on the gas property and the geometry of the solid surface, the heat transfer coefficient is

insensitive to the materials composition of the NWs.<sup>16</sup> As such, the discovered behavior of the heat transfer coefficient is expected to be universal, and applicable to any other NWs composed of different solid materials.

## CONCLUSIONS

By imaging the laser-heating induced metal–insulator phase transition along single, free-standing  $\text{VO}_2$  NWs, we determined the heat transfer coefficient between the NW and the gas environment over a wide range of pressure and down to the submicrometer scale. We found that the heat transfer coefficient behaves differently for nanoscale surface compared to at macroscopic scales: (1) at or slightly below ambient pressure, it is strongly pressure- and size-dependent, while for macroscopic-scale surfaces it is pressure insensitive. This is consistent with the prediction of the classical kinetic theory of gas. However, (2) at low pressures when the mean free path of gas molecules is comparable to the distance between the hot surface and heat sink, the heat transfer coefficient is much higher than theoretical predictions. We attribute this discrepancy to the relatively strong heat loss due to gas convection at this pressure range. It is also demonstrated that (3) the heat loss to gaseous environment from nanoscale solid surface can dominate over other heat loss channels such as through solid–solid interface. These findings have important implications to improving performance and thermal management of nanomaterial-based devices at miniaturized scales. In addition, the demonstrated laser thermography combined with phase transition of  $\text{VO}_2$  can serve as a general platform for quantitative control and evaluation of heat generation, transfer, and dissipation in nanoscale systems. For example, by attaching a  $\text{VO}_2$  NW to another single nanostructure “X”, the domain structure of the  $\text{VO}_2$  can be used as an accurate, nanoscale power-meter and thermometer to gauge energy exchange of “X” with the heat source and sink. This would enable quantification of many properties of single nanostructures that have been thus far extremely difficult to measure, such as thermal conductivity, specific heat, thermal diffusivity, and phase transition latent heat, etc.

## MATERIALS AND METHODS

**Nanowire Growth.** The  $\text{VO}_2$  NWs were synthesized using a modified version of the vapor transport method reported previously: bulk  $\text{VO}_2$  powder was placed in a quartz boat in the center of a horizontal tube furnace. The reaction product was collected on a Si substrate with a thermally grown  $\text{SiO}_2$  (100 nm) surface downstream from the source boat. The growth was carried out in the following condition: temperature  $\approx 1000^\circ\text{C}$ , Ar carrier gas flow rate  $\approx 4$  sccm, pressure  $\approx 5$  Torr, evaporation time  $\approx 6$  h. The size distribution, lattice structure and crystal orientation of these NWs were characterized by optical microscopy, scanning electron microscopy, X-ray diffraction, and

transmission electron microscopy. By carefully controlling the growth condition, some of the NWs grow out of the edge of the substrate forming strain-free cantilevers. The root of these  $\text{VO}_2$  NWs were firmly clamped and half embedded in the Si substrate. For  $\text{VO}_2$  NWs with submicrometer diameter, the M-I domains always line up one-dimensionally along the NW due to high energy cost of the M-I domain walls.

**Laser Thermography.** Bright- and dark-field optical images of  $\text{VO}_2$  were recorded using an optical microscope equipped with a color CCD camera. The laser heating of single, cantilevered NWs was carried out using a microscope with continuous-wave Ar ion laser (wavelength 514.5 nm). The stage can be moved in

the  $x$ - $y$  plane with respect to the laser spot, and the laser power is tuned by an assembly of half-wavelength plate, beam splitter, and neutral filters. The size of the focused laser spot is less than 2  $\mu\text{m}$  and the domain images were recorded using a black/white CCD camera. Prior to the measurements on each NW, the maximum safe laser power was determined by focusing at the tip of the NW, such that lower laser intensities were used in subsequent experiments to avoid damaging the NW (yet the laser needs to be strong enough to be able to activate the phase transition). For each data point, the laser focal depth and position were carefully adjusted to achieve a maximum M domain length so as to eliminate misalignment. A gas inlet pressure/flow controller (MKS 250E-4-A) equipped with a mechanical pump was used to control the gas pressure.

**Acknowledgment.** This work was supported by the U.S. Department of Energy Early Career Award DE-FG02-11ER46796. The materials synthesis part was supported by the National Science Foundation (NSF) under Grant No. CMMI-1000176.

**Supporting Information Available:** Measurement schematics and data processing. This material is available free of charge via the Internet at <http://pubs.acs.org>.

## REFERENCES AND NOTES

- Shen, S.; Narayanaswamy, A.; Chen, G. Surface Phonon Polaritons Mediated Energy Transfer between Nanoscale Gaps. *Nano Lett.* **2009**, *9*, 2909–2913.
- Kittel, A. Probing Near-Field Thermal Radiation. *Nat. Photonics* **2009**, *3*, 492–494.
- Rousseau, E.; Siria, A.; Jourdan, G.; Volz, S.; Comin, F.; Chevrier, J.; Greffet, J. Radiative Heat Transfer at the Nanoscale. *Nat. Photonics* **2009**, *3*, 514–517.
- Hochbaum, A. I.; Chen, R.; Delgado, R. D.; Liang, W.; Garnett, E. C.; Najarian, M.; Majumdar, A.; Yang, P. Enhanced Thermoelectric Performance of Rough Silicon Nanowires. *Nature* **2008**, *451*, 163–165.
- Boukai, A. I.; Bunimovich, I.; Tahir-Kheli, J.; Yu, J.-K.; Goddard, W. A.; Heath, J. R. Si Nanowires as Efficient Thermoelectric Materials. *Nature* **2008**, *451*, 168–171.
- Lee, J.; Galli, G. A.; Grossman, J. C. Nanoporous Si as an Efficient Thermoelectric Material. *Nano Lett.* **2008**, *8*, 3750–3754.
- He, Y.; Donadio, D.; Lee, J.; Grossman, J. C.; Galli, G. Thermal Transport in Nanoporous Silicon: Interplay between Disorder at Mesoscopic and Atomic Scales. *ACS Nano* **2011**, *5*, 1839–1844.
- Huang, M. H.; Mao, S.; Feick, H.; Yan, H. Q.; Wu, Y. Y.; Kind, H.; Weber, E.; Russo, R.; Yang, P. D. Room-Temperature Ultraviolet Nanowire Nanolasers. *Science* **2001**, *292*, 1897–1899.
- van Vugt, L. K.; Ruhle, S.; Vanmaekelbergh, D. Phase-correlated Nondirectional Laser Emission from the End Facets of a ZnO Nanowire. *Nano Lett.* **2006**, *6*, 2707–2711.
- She, J.; Xiao, Z.; Yang, Y.; Deng, S.; Chen, J.; Yang, G.; Xu, N. Correlation between Resistance and Field Emission Performance of Individual ZnO One-Dimensional Nanostructures. *ACS Nano* **2008**, *2*, 2015–2022.
- Strelcov, E.; Lilach, Y.; Kolmakov, A. Gas Sensor Based on Metal-Insulator Transition in VO<sub>2</sub> Nanowire Thermistor. *Nano Lett.* **2009**, *9*, 2322–2326.
- Jensen, K.; Weldon, J.; Garcia, H.; Zettl, A. Nanotube Radio. *Nano Lett.* **2007**, *7*, 3508–3511.
- Sazonova, V.; Yaish, Y.; Ustunel, H.; Roundy, D.; Arias, T. A.; McEuen, P. L. A Tunable Carbon Nanotube Electromechanical Oscillator. *Nature* **2004**, *431*, 284–287.
- Chan, H. B.; Aksyuk, V. A.; Kleiman, R. N.; Bishop, D. J.; Capasso, F. Quantum Mechanical Actuation of Microelectromechanical Systems by the Casimir Force. *Science* **2001**, *291*, 1941–1944.
- Beskok, A.; Karniadakis, G. E. A Model for Flows in Channels, Pipes, and Ducts at Micro and Nano Scales. *Microscale Thermophys. Eng.* **1999**, *3*, 43–77.
- Lafferty, J. M. *Foundations of Vacuum Science and Technology*; John Wiley & Sons, Inc.: New York, 1998; pp 44–73.
- Berglund, C. N.; Guggenheim, H. J. Electronic Properties of VO<sub>2</sub> near the Semiconductor–Metal Transition. *Phys. Rev.* **1969**, *185*, 1022–1033.
- Eyert, V. The Metal–Insulator Transitions of VO<sub>2</sub>. A Band Theoretical Approach. *Ann Phys. (Berlin, Ger.)* **2002**, *11*, 650–702.
- Wu, J.; Gu, Q.; Guiton, B. S.; de Leon, N. P.; Ouyang, Lian; Park, H. Strain-Induced Self-Organization of Metal-Insulator Domains in Single-Crystalline VO<sub>2</sub> Nanobeams. *Nano Lett.* **2006**, *6*, 2313–2317.
- Cao, J.; Ertekin, E.; Srinivasan, V.; Fan, W.; Huang, S.; Zheng, H.; Yim, J. W. L.; Khanal, D. R.; Ogletree, D. F.; Grossman, J. C.; *et al.* Strain Engineering and One-Dimensional Organization of Metal-Insulator Domains in Single-Crystal Vanadium Dioxide Beams. *Nat. Nanotechnol.* **2009**, *4*, 732–737.
- Guiton, B. S.; Gu, Q.; Prieto, A. L.; Gudixsen, M. S.; Park, H. Single-Crystalline Vanadium Dioxide Nanowires with Rectangular Cross Sections. *J. Am. Chem. Soc.* **2005**, *127*, 498–499.
- Dickins, B. G. The Effect of Accommodation on Heat Conduction through Gases. *Proc. R. Soc. London, Ser. A* **1934**, *143*, 517–540.
- Smith, D. L. *Thin Film Deposition: Principles and Practice*; McGraw Hill: New York, 1995; pp 25–32.
- Langmuir, I. Convection and Conduction of Heat in Gases. *Phys. Rev.* **1912**, *34*, 401–422.
- Brody, I.; Korosy, F. Convection and Conduction of Heat in Gases. *J. Appl. Phys.* **1939**, *10*, 584–596.
- Strand, J.; Vengar, A. Stefan's Measurement of the Thermal Conductivity of Air. *Eur. J. Phys.* **1984**, *5*, 9–12.
- Incropera, F. P.; DeWitt, D. P. *Introduction to Heat Transfer*; John Wiley & Sons: New York, 2002; pp 516–518.

## Supporting Information of

### Heat Transfer across the Interface between Nanoscale Solids and Gas

Measurement schematics and data processing. This material is available free of charge *via* the Internet at <http://pubs.acs.org>.

**Figure S1.** Schematic of the laser heating system for the laser thermography experiment. Abbreviations in the figure are: M: mirror, BS: beam splitter, PBS: polarizing beam splitter,  $\lambda/2$ : half-wave plate, NF: neutral filter.

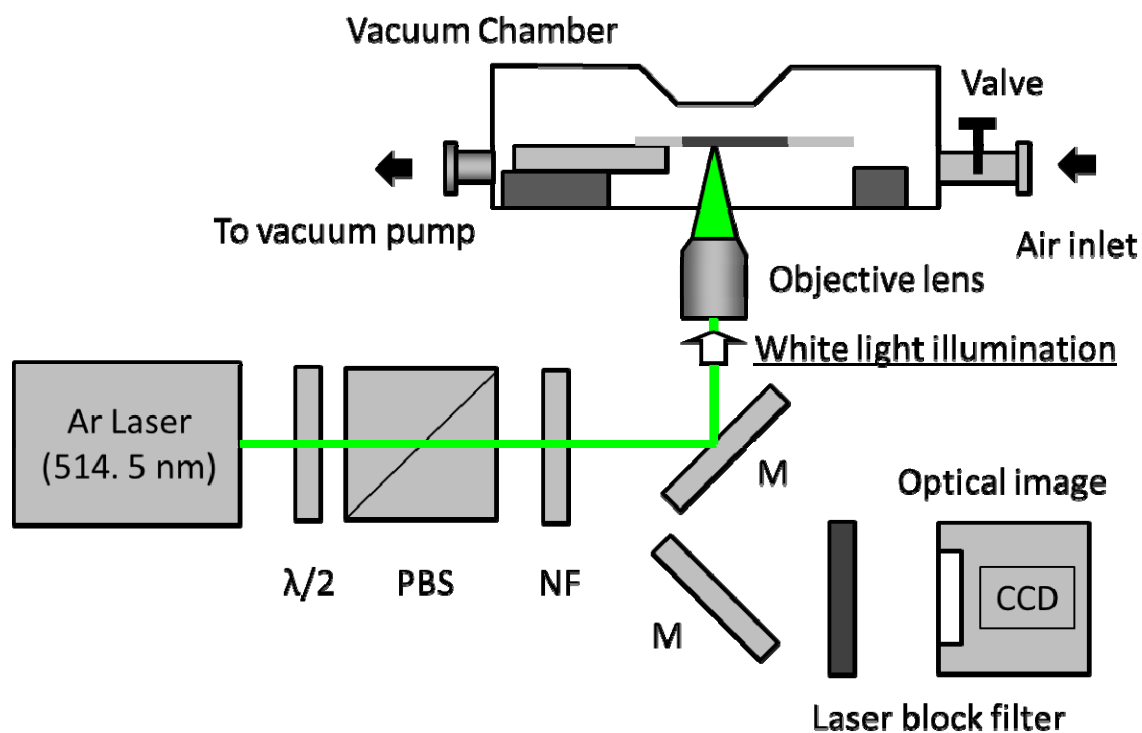
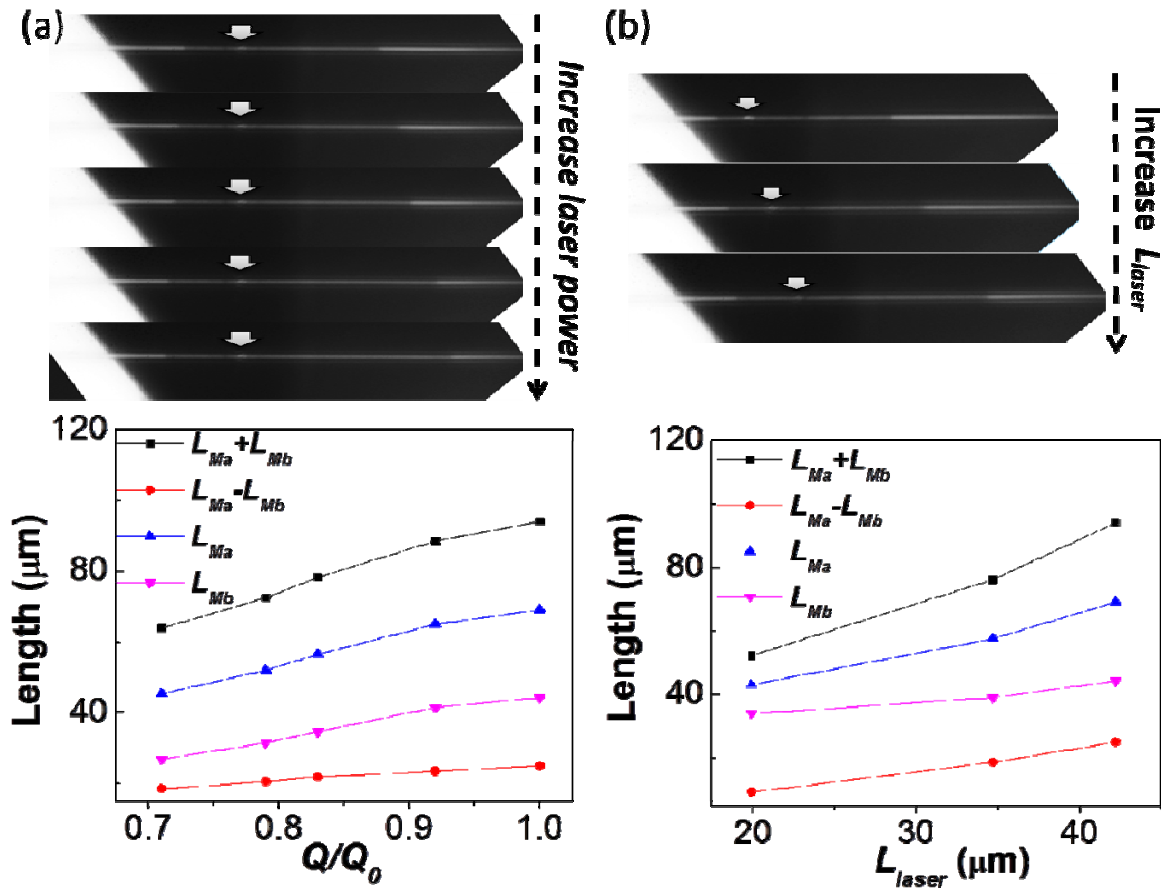


**Figure S2.** The laser power and laser position dependent domain structure at a pressure of 0.02 torr. The arrows indicate the position of the focused laser spot.



**Data fitting.** For a VO<sub>2</sub> NW with width  $D$  at pressure  $P$ , the M domain lengths  $L_{Ma}$  and  $L_{Mb}$  were experimentally measured for different combinations of  $(L_{laser}, Q/Q_0)$ . The deviation between the  $L_{Ma}$  and  $L_{Mb}$  theoretically predicted from Eq.(4) and the experimentally measured ones is given by

$$\eta(h, Q_0) = \sum_{L_{laser}, Q/Q_0} \left[ \left( L_{Ma}^{measured} - L_{Ma}^{theory}(h, Q_0) \right)^2 + \left( L_{Mb}^{measured} - L_{Mb}^{theory}(h, Q_0) \right)^2 \right].$$

The least-square method was used to numerically find the best  $h$  and  $Q_0$  values that minimize  $\eta(h, Q_0)$  for each set of experimental data at the  $P$  and  $D$  values. The obtained  $h$  was then plotted as a function of  $P$  and  $D$  in Fig.3.